J. Hydrol. Hydromech., 65, 2017, 4, 410–425
DOI: 10.1515/johh-2017-0038

Simulations of coupled non-isothermal soil moisture transport and evaporation fluxes in a forest area

Wei Shao[1], Ye Su[2], Jakub Langhammer[2*]

[1] College of Hydrometeorology, Nanjing University of Information Science and Technology, Nanjing 210044, Jiangsu, China.
[2] Department of Physical Geography and Geoecology, Faculty of Science, Charles University, Albertov 6, 128 43 Prague 2, Czech Republic.
[*] Corresponding author. Tel.: +420-221951415. Fax: +420-221951415. E-mail: jakub.langhammer@natur.cuni.cz

Abstract: This study focuses on the quantification of non-isothermal soil moisture transport and evaporation fluxes in vegetated area. A one-dimensional numerical model is developed by integrating a multi-phase flow model with a two-layer energy-balance model. The non-isothermal multi-phase flow model solves four governing equations for coupled air, vapour, moisture, and heat transport in soil porous medium. The two-layer energy balance model estimates evaporation fluxes from transpiration, interception, and soil surface. The model was implemented to an oak forest area in Missouri, USA. For model calibration and validation, measurements of energy fluxes, soil moisture, and soil temperature were used. The proposed model is compared with a simple model that couples the Penman-Monteith equation with the Richards' equation. The results indicate that the simple model underestimate the total evaporation rate. On the contrary, the proposed model includes a more detailed description of energy transfer, which could improve the accuracy in estimating evaporation rates. The proposed model could be a promising tool to quantify the energy and moisture fluxes in a soil-vegetation-atmosphere continuum in vegetated area.

Keywords: Soil–vegetation–atmosphere transfer model; Evaporation flux; Soil moisture transport; Forest meteorology.

INTRODUCTION

In vegetated area, evaporation generally consists of three components: interception evaporation, transpiration, and soil evaporation (Savenije, 2004). The variation of evaporation fluxes is mutually affected by meteorological fluctuation, vegetation dynamics, and soil moisture stress (Entekhabi et al., 1996; Rodriguez-Iturbe, 2000; Šír et al., 2001). The interaction between soil moisture dynamics with evaporation fluxes can be summarized as follows. Interception diminishes the precipitation that arrives at the soil surface, causing more gradual infiltration (Dohnal et al., 2014). Transpiration is directly conducted through the stomata of leaves and simultaneously consumes soil moisture from the root zone. Soil evaporation drives exfiltration, water phase change, and upward vapour flow in the soil porous medium. In addition, the dynamics of moisture and temperature at soil surface mutually dictate the variations of albedo, emissivity, and vapour pressure, which influence energy budget and evaporation fluxes (Eltahir, 1998; Seneviratne et al., 2010). Therefore, quantification of land-atmosphere interaction needs an integrated model incorporating theories of soil physics, vegetation physiology, and atmospheric science to simulate the energy and moisture transport in a soil–vegetation–atmosphere transfer (SVAT) continuum (Gran et al., 2011; Overgaard et al., 2006).

The descriptions of evaporation processes are different in SVAT models. Coupling the Penman-Monteith equation with the Richards' equation is the basis of many software to calculate the interaction between actual evaporation and soil moisture dynamics, e.g., Hydrus-1D (Šimůnek et al., 2013). However, the application of the analytical evaporation equations needs pre-define the soil surface temperature and ground heat flux, and the thermal energy transport was not explicitly simulated (Varado et al., 2006; Were et al., 2008; Yin et al., 2014). Many studies, however, suggested that the evaporation fluxes can be strongly related with biophysical process of vegetation, and dynamics of soil moisture and soil temperature (Garcia Gonzalez et al., 2012; Guimberteau et al., 2014; Kollet and Maxwell, 2008; Saito et al., 2006). The current SVAT models emphases on improving the physiological processes (Bonan et al., 2014; Gran et al., 2011; Overgaard et al., 2006), while the processes descriptions may be further improved by including the non-isothermal soil moisture transport.

The soil moisture and the energy transport can be simulated by multi-phase flow models solving the governing equations for moisture, air, vapour, and heat transport in soil (Garcia Gonzalez et al., 2012). The non-isothermal multi-phase flow models have demonstrated a high accuracy in simulating soil temperature, moisture content, and evaporation rate (Grifoll et al., 2005; Smits et al., 2012; Zeng et al., 2011). However, the existing applications are still limited in bare soil for either short-time period studies (i.e., a few days) (Davarzani et al., 2014) or indoor chamber evaporation experiments (Grifoll, 2013; Mosthaf et al., 2011; Smits et al., 2012). The non-isothermal multi-phase flow models enable a more complete description of both soil hydrology and thermodynamics processes, and they also have potential to apply in the vegetated soils.

In this study, a one-dimensional model is developed by integrating a non-isothermal multi-phase flow model with a two-layer energy-balance model to quantify the interactions between evaporation fluxes, soil hydrology, and thermodynamics. The proposed model is implemented to an oak forest area in Missouri, USA. The detailed measurements of energy fluxes, soil moisture, and soil temperature are used for model calibration and validation. The analyses are focused on i) quantifying the dynamics of moisture and temperature in the soil in response to various meteorological conditions, and ii) partitioning the evaporation into transpiration, soil evaporation, and interception evaporation.

STUDY SITE

The study area is located at 38.7° N, 92.2° W (with elevation 219 m a.s.l.) in Missouri, USA. The land cover is deciduous broadleaf forest with tree species of oak hickory. The site is uniquely located in a transitional zone between the central hardwood region and the central grassland region of the US. The climate condition is warm temperate-fully humid with hot summer. Field experiment was conducted by Oak Ridge National Laboratory, aiming to investigate the evaporation fluxes under varying meteorological and environmental conditions.

The study period is from 2 August 2004 (DoY215) to 26 September 2004 (DoY270) in the early autumn season. The leaf area index (LAI) of vegetation cover is 5.0, and the canopy height is 24 m. The soil is Weller silt loam with bulk density of 1.5 g/cm^3. An eddy covariance flux tower was installed at the 30 m height to measure the sensible and latent heat fluxes. The total evaporation rate can be gained from the measured latent heat flux. The net radiation was measured from a four-component net radiometer. In the soil, temperature sensors were buried at the depths of 4 cm, 8 cm, 32 cm, and 64 cm, and three time-domain reflectometers (TDRs) were installed to measure the soil moisture content at the depth of 8, 32, and 64 cm. All above-mentioned data were collected in a 30-minute interval. The data is available from the FLUXNET Database (http://fluxnet.ornl.gov/site/967).

MODEL DESCRIPTION

Two-layer energy-balance

The energy-balance is calculated for two layers that consist of a canopy layer and a soil surface layer. The measured net radiation $\mathbf{R}^{net}$ (W m^{-2}) was partitioned into two components following the Beer's law (Zhou et al., 2006):

$$\mathbf{R}_{sur}^{net} = \mathbf{R}^{net} \exp(-C_r I_{\mathrm{LAI}}) \quad (1)$$

$$\mathbf{R}_{can}^{net} = \mathbf{R}^{net} \left[1-\exp(-C_r I_{\mathrm{LAI}})\right] \quad (2)$$

where subscripts "can" and "sur" indicate canopy layer and soil surface layer, I_{LAI} (–) is the leaf area index, and c_r (–) is the extinction coefficient of the vegetation for net radiation. The net radiations are further transferred into specific forms in the two layers (Davarzani et al., 2014; Mosthaf et al., 2011):

$$\mathbf{R}_{can}^{net} = \lambda E_{can} + H_{can} \quad (3)$$

$$\mathbf{R}_{sur}^{net} = \lambda E_{sur} + H_{sur} + G_H \quad (4)$$

where λE (W m^{-2}) is the latent heat, H (W m^{-2}) is the sensible heat, G_H (W m^{-2}) is the ground heat flux, and λ ($\approx 2.45\times10^6$ J kg^{-1}) is the latent heat for vaporization, which is associated with the evaporation rate E (kg m^{-2} s^{-1}).

The energy-balance equation for canopy layer (Eq. 3) is similar to many SVAT models (e.g., Choudhury and Monteith, 1988; Colaizzi et al., 2012; Xin and Liu, 2010), which neglects the influence of other energy components (e.g., canopy heat storage and photosynthesis) on energy transfer. The energy components of ground heat, sensible heat, and latent heat fluxes are calculated in analogy to a two-layer electrical resistance network with equations given in Table 1. The sensible and latent heat fluxes are driven by gradients of temperature and vapor pressure between the interfaces of soil, canopy, and atmosphere respectively (Choudhury and Monteith, 1988; Xin and Liu, 2010). The calculation of resistance coefficients (given in the Appendix) considers the influence of multiple environmental stresses.

Canopy interception, transpiration, and root water uptake

Interception occurs when rainfall is captured by surface storage (e.g., vegetation canopy, roofs, etc.) before reaching the soil surface (Savenije, 2004). The water storage of interception in the canopy layer represents the depth of rainwater stored on leaves and branches that is expressed by (Eltahir and Bras, 1993; Ivanov et al., 2008; Rutter et al., 1971):

$$\frac{dS_C}{dt} = (1-\tau_{rain}) q_{rain} - q_{drip} - E_i/\rho_w \quad (5)$$

where S_C (m) is the interception storage, t (s) is time, E_i (kg m^{-2} s^{-1}) is the interception evaporation, ρ_w (kg m^{-3}) is the density of liquid water, q_{rain} (m s^{-1}) is the rainfall intensity, $(1-\tau_{rain})q_{rain}$ is the intercepted rainwater, τ_{rain} (–) is a coefficient that denotes the fraction of rainfall that directly penetrates through canopy and reaches soil surface:

$$\tau_{rain} = \exp\left(-0.5 I_{\mathrm{LAI}}\right) \quad (6)$$

Table 1. Formulations of energy fluxes and resistance network.

Position	Sensible heat	Latent heat	Energy network
Canopy	$H_{can} = \rho_a c_p \dfrac{T_{veg} - T_{can}}{r_{ac}}$	$\lambda E_{can} = \dfrac{\rho_a c_p}{\gamma} \dfrac{e^*_{veg} - e_{can}}{r_{ac} + r_c}$	$\mathbf{R}_{can}^{net} = \lambda E_{can} + H_{can}$
Soil surface	$H_{sur} = \rho_a c_p \dfrac{T_{sur} - T_{can}}{r_{as}}$	$\lambda E_{sur} = \dfrac{\rho_a c_p}{\gamma} \dfrac{e_{sur} - e_{can}}{r_{as} + r_s}$	$\mathbf{R}_{sur}^{net} - G_H = \lambda E_{sur} + H_{sur}$
Atmosphere	$H = \rho_a c_p \dfrac{T_{can} - T_{atm}}{r_a}$	$\lambda E = \dfrac{\rho_a c_p}{\gamma} \dfrac{e_{can} - e_{atm}}{r_a}$	$\mathbf{R}^{net} - G_H = \lambda E + H$
Energy network	$H = H_{can} + H_{sur}$	$\lambda E = \lambda E_{can} + \lambda E_{sur}$	$\mathbf{R}^{net} = \mathbf{R}_{can}^{net} + \mathbf{R}_{sur}^{net}$

Note: subscript "atm", "can", and "sur" represent atmospheric layer, canopy layer, and soil surface; subscript "veg" represents vegetation foliage; T (K) is the temperature; e (Pa) is the vapour pressure; e^* (Pa) is the saturation vapour pressure; c_p (J kg^{-1} K^{-1}) is the specific heat capacity of moist air under a constant pressure; ρ_a (1.013 kg m^{-3}) is the density of the air; γ (PaK^{-1}) is the psychometric constant; r_a, r_{ac} and r_{as} (s m^{-1}) are the aerodynamic resistances between canopy and reference height, between foliage and canopy air, and between soil surface and canopy air respectively; and r_s and r_c are the soil surface resistance and the bulk stomatal resistance of the canopy layer.

where q_{drip} (m s^{-1}) is the canopy drainage rate:

$$q_{drip} = K_C \exp\left[g_C \left(S_C - S_{C\max} \right) \right] \tag{7}$$

where g_C (m^{-1}) is an exponential decay parameter, $S_{C\max}$ (m) is the capacity of canopy water storage, and K_C (m s^{-1}) is the drainage rate when the water storage reaches to its capacity.

E_i (kg m^{-2} s^{-1}) is the interception evaporation, which is one component of E_{can} (Eltahir and Bras, 1993):

$$E_i = \left(S_C / S_{C\max} \right)^{2/3} E_{can} \tag{8}$$

The assumption in Eq. 8 is that the interception can alter the transpiration rate E_t without feedback to total evaporation rate from canopy E_{can}. When the interception is existing, the transpiration rate E_t (kg m^{-2} s^{-1}) is then calculated by:

$$E_t = E_{can} - E_i \tag{9}$$

The transpiration rate is equal to the root water uptake. In wet soils, the distribution of water uptake is directly linked to root distribution described by an exponential function (Feddes et al., 2001):

$$g_{root} = e^{-cz} \tag{10}$$

where g_{root} (–) is the root density distribution, z (m) is the soil depth, and c (m^{-1}) is a fitting parameter.

In water-limited soil, the diminished water uptake rate of dryer soil layer can be compensated by the enhanced water uptake from wetter layer (van Dijk and Bruijnzeel, 2001), the spatial distribution of root water uptake will be attributed to the variations of soil moisture content and root density distribution (Varado et al., 2006):

$$Q_R(h_w, z) = \frac{\alpha_R(h_w, z) g_{root}(z)}{\int_{d_{root}} \alpha_R(h_w, z) g_{root}(z) dz} E_t \tag{11}$$

where Q_R (kg m^{-3} s^{-1}) is the root water uptake rate, h_w (m) is the pore water pressure head, d_{root} (m) is the rooting depth, and α_R (–) is an empirical reduction function (Feddes et al., 2001):

$$\alpha_R(h_w) = \begin{cases} 0, & h_w \le h_{wilting} \\ \dfrac{h_w - h_{wilting}}{h_{field} - h_{wilting}}, & h_{wilting} < h_w < h_{field} \\ 1, & h_w \ge h_{field} \end{cases} \tag{12}$$

where $h_{wilting}$ (–150 m) and h_{field} (–3.3 m) are the pressure head on permanent wilting point and field capacity respectively.

The net rainfall $q_{w,sur}$ for soil surface infiltration is a sum of the direct throughfall $\tau_{rain} q_{rain}$ and the canopy drainage q_{drip}:

$$q_{w,sur} = \tau_{rain} q_{rain} + q_{drip} \tag{13}$$

Non-isothermal multi-phase flow in soil porous medium

The moisture and energy transport in soil porous medium are simulated within a non-isothermal multi-phase flow model proposed by Grifoll et al. (2005). In this study, the model was extended by considering the root water uptake that links to the vegetation transpiration. The coupled air, liquid water, vapour, and heat transport in soil porous medium can be expressed by three mass-balance equations and one energy-balance equation (Grifoll et al., 2005):

$$\frac{\partial \rho_a \theta_a}{\partial t} + \frac{\partial (\rho_a q_a)}{\partial z} = Q_E \tag{14}$$

$$\frac{\partial \rho_w \theta_w}{\partial t} + \frac{\partial (\rho_w q_w)}{\partial z} = -Q_E - Q_R \tag{15}$$

$$\frac{\partial \theta_a \rho_v}{\partial t} + \frac{\partial (\rho_v q_a + \theta_a J_v)}{\partial z} = Q_E \tag{16}$$

$$\frac{\partial [\theta_w \rho_w c_w + \theta_a \rho_a c_a + (1-\phi)\rho_s c_s] T}{\partial t} + \frac{\partial [\rho_w c_w q_w + \rho_a c_a q_a + \theta_a J_v (c_v - c_{a,dry})] T}{\partial z} + \frac{\partial J_h}{\partial z} = -\lambda Q_E - c_w Q_R T \tag{17}$$

where ρ (kg m^{-3}) is the mass density, with subscripts of *a*, *w*, *v*, and *s* denote the air, liquid water, vapour, and solid phase respectively; θ_w and θ_a (m^3 m^{-3}) are the volumetric content of moisture and air, ϕ (m^3 m^{-3}) is the porosity, Q_E (kg m^{-3} s^{-1}) is the water phase change rate caused by vaporization and condensation in the soil, Q_R (kg m^{-3} s^{-1}) is the root water uptake rate, q_w and q_a (m s^{-1}) are the specific discharge of water flow and air flow, J_v (kg m^{-2} s^{-1}) is the hydrodynamic dispersion (dispersion and diffusion) of vapour in soils, T (°C) is the temperature of soil, c (J kg^{-1} K^{-1}) is the specific heat capacity with different values for solids, liquid water, dry air and water vapour (c_s = 870 J kg^{-1} K^{-1}, c_w = 4180 J kg^{-1} K^{-1}, c_a = 1006 J kg^{-1} K^{-1}, and c_v = 1996 J kg^{-1} K^{-1}), and J_h (W m^{-2}) is the heat flux density in soil caused by the thermal conduction and dispersion.

In unsaturated soil, air may freely escape from soil to atmosphere, so that the air pressure along the soil profile may be constant (Grifoll, 2013; Grifoll et al., 2005). Under such condition, air flow is driven by two mechanisms: the changes of moisture content cause the changes of volumetric air content, and the air density ρ_a varies due to expansion or contraction effects caused by the changes of vapour density ρ_v:

$$\rho_a = \frac{p_{atm}}{R T_k} \left[\frac{\rho_v}{\rho_a} \frac{1}{M_w} + \left(1 - \frac{\rho_v}{\rho_a} \right) \frac{1}{M_a} \right]^{-1} \tag{18}$$

$$\rho_v = \rho_{vs} H_{re} = \rho_{vs} \exp\left(\frac{h_w g M_w}{R T_k} \right) \tag{19}$$

$$\rho_{vs} = \frac{0.001}{T_k} \exp\left(31.37 - \frac{6015}{T_k} - 7.925 \times 10^{-3} T_k \right) \tag{20}$$

where p_{atm} (kPa) is the atmospheric pressure, R (8.3145 J mol^{-1} K^{-1}) is the gas constant, g (9.81 m s^{-2}) is the gravitational acceleration, M_w (18.02 g mol^{-1}) and M_a (28.96 g mol^{-1}) are the molar weight of water and dry air, H_{re} is the relative

humidity, T_k (K) is the thermodynamic temperature, and ρ_{vs} (kg m^{-3}) is the saturated vapour density.

Neglecting the hysteresis effect and preferential flow, the specific discharge of liquid water flow (positive upward) can be calculated by the Darcy's law (Pinder and Celia, 2006):

$$q_w = -K_w\left(\frac{\partial h_w}{\partial z}+1\right) \tag{21}$$

where K_w (m s^{-1}) is the hydraulic conductivity. The Mualem-van Genuchten model is used to express water retention curve and hydraulic conductivity function as given in Table 2 (van Genuchten, 1980). The thermal liquid water flow is neglected (see Eq. 21). Many studies showed that liquid water flow is driven by capillary gradient and gravity, and the influence of temperature gradient on liquid water flow is negligible (Davarzani et al., 2014; Pinder and Celia, 2006; Smits et al., 2011).

For calculating the vapour transport in soil porous medium, the hydrodynamic vapour dispersion term J_v is given as (Milly, 1984):

$$J_v = -\left[\frac{D_a}{\varsigma_a}+D_{mG}^M\right]\frac{\partial \rho_v}{\partial z} \tag{22}$$

where D_a and D_{mG}^M (m^2 s^{-1}) are the vapour diffusion and mechanical dispersion, respectively (Table 2), and ς_a (–) is the tortuosity (Grifoll et al., 2005):

$$\varsigma_a = \phi^{2/3}/\theta_a \tag{23}$$

The heat flow equation (Eq. 17) is formulated based on the assumption of local thermodynamic equilibrium: the temperatures of three phases (i.e., water, air, and soil solid matrix) are equivalent (Grifoll, 2013; Mosthaf et al., 2011; Parlange et al., 1998), which holds if the preferential flow is negligible. The advection thermal transport is caused by the mass transport of water and air. The phase change and root water uptake are formulated as source/sink terms of λQ_E and $c_W Q_R T$ respectively. Additionally, the thermal conduction and dispersion in soil porous medium may be expressed as (Saito et al., 2006):

$$J_h = -\left[K_H+\theta_w\rho_w c_w D_{mL}^H\right]\frac{\partial T}{\partial z} \tag{24}$$

where D_{mL}^H (m^2 s^{-1}) is the thermal dispersion coefficient induced by water flow, and K_H (W m^{-1}K^{-1}) is the thermal conductivity (Table 2).

Model coupling approaches and numerical strategies

The moisture and energy fluxes estimated by the two-layer energy-balance equations were used to specify the boundary conditions of the multi-phase flow model (Section "Model description"). For the water flow equation, a net rainfall $q_{w,sur}$ is set as the upper boundary (Eq. 13), and a gravitational drainage is specified for the lower boundary assuming the groundwater table far below the computational domain. Transpiration is linked to root water uptake that is specified as a sink term in the water flow equation. For vapour flow equation (Eq. 16), the upper boundary is the soil surface evaporation rate E_{sur} that is obtained from Eq. 4. At the lower boundary of soil domain, both vapour flow and air flow were specified as zero-flux.

The boundary conditions of heat flow equation (Eq. 17) include both thermal advection and conduction. Thermal advection is mainly driven by liquid water flow of drainage and infiltration. At the upper boundary, we assume the temperature of the rainwater is equal to the atmospheric temperature at 30 m height. The infiltration on the soil surface and drainage from soil bottom cause thermal advection in the soil heat flow equation (Eq. 17). Thermal conduction at the upper boundary is set to the ground heat flux and at the lower boundary is set to the zero-gradient condition.

The energy fluxes and soil physical processes are strongly coupled. Specifically, the latent heat flux λE_{sur} is corresponding to the soil surface evaporation rate that is specified as the upper boundary for the vapour flow equation. The calculated transpiration rate E_t drives the root water uptake distribution as a sink term Q_R in the water flow equation. The ground heat flux G_H is used to specify the heat flux at the upper boundary of the soil. In turn, the temperature and moisture dynamics on the soil surface will affect the energy fluxes.

Table 2. Formulations of the transport terms and coefficients.

Constitutive law	Equation	Parameter notation	Reference
Soil hydraulic function	$\Theta = \frac{\theta_w-\theta_{wr}}{\theta_{ws}-\theta_{wr}} = \begin{cases}\left[1+\lvert\alpha_{\mathrm{VG}}h_w\rvert^{n_{\mathrm{VG}}}\right]^{-m_{\mathrm{VG}}}, & h_w<0\\ 1, & h_w\geq 0\end{cases}$	θ_{wr} and θ_{ws} (m^3 m^{-3}) are the residual and saturated moisture content; Θ (–) is the degree of saturation.	(van Genuchten, 1980; Zeng et al., 2011)
	$K_w = K_{ws}\Theta^{l_{\mathrm{VG}}}\left[1-\left(1-\Theta^{1/m_{\mathrm{VG}}}\right)^{m_{\mathrm{VG}}}\right]^2$	α_{VG}, l_{VG}, m_{VG}, and n_{VG} are fitting parameters ($m_{\mathrm{VG}}=1/n_{\mathrm{VG}}$); K_{ws} (m s^{-1}) is the saturated hydraulic conductivity	
Vapour diffusion	$D_a = 2.12\times10^{-5}\left(\frac{T_k}{273.15}\right)^2$	T_k (K) is the absolute thermal temperature	(Smits et al., 2012)
Vapour dispersion	$D_{mG}^M = \alpha_L\lvert v_a\rvert$	$v_a = q_a/\theta_a$ is the pore velocity of air flow; α_L (m) is a longitudinal dispersivity	(Grifoll et al., 2005)
Thermal diffusion	$K_H = b_1+b_2\theta_w+b_3\theta_w^{0.5}$	b_1, b_2, and b_3 are fitting parameters	(Chung and Horton, 1987; Grifoll et al., 2005)
Thermal dispersion	$D_{mL}^H = \alpha_H\lvert v_w\rvert$	$v_w = q_w/\theta_w$ is the pore velocity of water flow; α_H (m) is the thermal dispersivity	(Grifoll, 2013)

The mathematical framework is numerically solved by an author-developed script under Python 2.7 programming language. Specifically, the governing equations in multi-phase flow model compose a fully-coupled partial differential equations system. The iteration approach proposed by Grifoll (2013) is used. The equations of air, vapour, and heat transport are solved by the Crank-Nicholson finite difference method, and the Richards equation is solved by a fully-implicit finite difference method (Celia et al., 1990; Pinder and Celia, 2006).

The model coupling is achieved by iteratively implementing the estimated evaporation and ground heat flux as the upper boundary of the soil, thereafter the simulated soil moisture content and temperature on the soil surface are used to recalculate the energy and evaporation fluxes. The numerical errors of soil moisture and temperature are controlled by the iteration technique with tolerable errors of 0.0001 and 0.01°C, respectively. The time step is constrained in a range of 0.005–5 min to ensure sufficient computational efficiency.

MODEL SET-UP AND PARAMETERIZATION

The measurements of net radiation, rainfall, atmospheric temperature, wind speed, and air humidity at the height of 30 m above the ground are used as model input (Fig. 1).

Model performance is evaluated by comparing simulations with measurements, including the energy fluxes of latent heat, sensible heat, and ground heat fluxes, as well as soil temperature and soil moisture content at different soil depths. Taken the soil moisture content as an example, the bias and root-mean-square error (RMSE) may be calculated as follows:

$$\text{Bias} = \frac{1}{N}\sum_{n=1}^{N}\left(\theta_{sim} - \theta_{obs}\right) \tag{25}$$

$$\text{RMSE} = \sqrt{\frac{1}{N}\sum_{n=1}^{N}\left(\theta_{sim} - \theta_{obs}\right)^2} \tag{26}$$

where θ_{sim} and θ_{obs} are the simulated and observed values (e.g., soil moisture content θ), and N is the number of values that used for comparison.

The parametrization of resistance coefficients is given in Appendix. Specifically, the aerodynamic resistance coefficients are calculated based on previous studies (Choudhury and Monteith, 1988; Xin and Liu, 2010), which are related with wind speed, canopy height, and surface roughness. The bulk stomatal resistance is calculated by the Jarvis-Stewart model accounting the influence of multiple environmental stresses of solar radiation, atmosphere temperature, vapour pressure deficit, and soil moisture stress on transpiration (Jarvis, 1976; Stewart, 1988). The root density distribution is decreasing from 1.0 (on the soil surface) to a very small value (at the lower boundary) following an exponential function with a coefficient *c* (Eq. 10) of 4.0. Soil surface resistance adopts the exponential function proposed by van de Griend and Owe (1994), which links the soil evaporation rate with the soil moisture at 1 cm depth.

The interception can reduce the amount and intensity of rainfall that reaches soil surface. The interception parameters for deciduous broadleaf forest area are adopted from Ivanov et al. (2008), and the interception storage $S_{C\max}$ is set to 5 mm as a typical value that is often used for the long-term water balance in the forest area (Gerrits et al., 2009) (Table 3). For the simulation of water flow in soils, most of the parameters adopted the typical values of silt loam (van Genuchten et al., 1991), including the saturated hydraulic conductivity K_{ws}, α_{VG} and the residual and saturated soil moisture content θ_{wr} and θ_{ws} (see Table 3). The soil thermal parameters given in Table 3 are also specified as the default parameter values of silt loam soil (Chung and Horton, 1987; Sakai et al., 2011).

The study period was split into two parts, one for model calibration (DoY 215-235) and another for model validation (DoY 235-270) (see Fig. 1). The values of calibrated parameters are shown in Table 3. The fitting parameter n_{VG} is calibrated according to the soil moisture response, and its value is 1.75 for upper layer soil (0–50 cm) and 1.35 for lower layer soil (50–100 cm). The extinction coefficient C_r can dictate the partitioning of the net radiation energy, and it is calibrated according to the measurements of soil temperature, latent heat, and ground heat fluxes. For the day-time, C_r is calibrated to

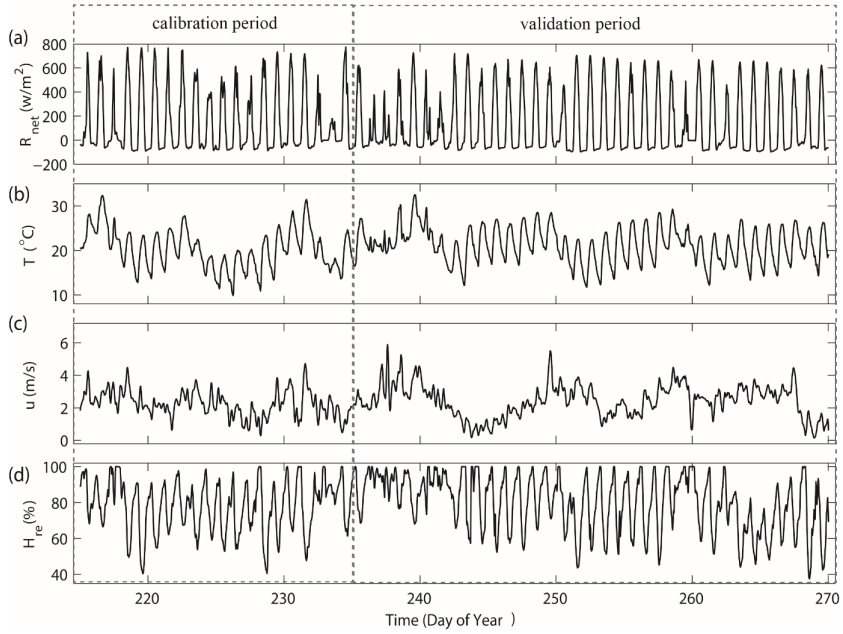

Fig. 1. Measured meteorological forcing data of (a) net radiation, (b) atmospheric temperature, (c) wind speed, and (d) air humidity in the study area over the period of DoY 215-DoY 270 in 2004. The calibration and validation periods are illustrated respectively.

Table 3. Parameters for soil hydraulic and canopy properties in non-isothermal soil multi-phase flow model and canopy interception module respectively.

Soil hydraulic parameter					
Depth (m)	θ_{wr} (–)	θ_{ws} (–)	K_{ws} (m/s)	α_{VG} (m^{-1})	n_{VG} (–)
0–0.5	0.067	0.45	1.25×10^{-6}	0.2	1.75
0.5–1.0	0.067	0.45	1.25×10^{-6}	0.2	1.35
Soil thermal parameter					
Depth (m)	b_1 (–)	b_2 (–)	b_3 (–)	α_L (m)	α_H (m)
0–1.0	0.243	0.393	1.534	0.1	0.1
Canopy interception parameter					
	$S_{C\max}$ (mm)	C_r (day / night time) (–)	K_C (mm/h)	g_C (–)	
	5	0.4 /0.08	0.18	3.9	

Note: θ_{wr} and θ_{ws} - residual and saturated moisture content; K_{ws} - saturated hydraulic conductivity; α_{VG}, n_{VG} - fitting parameters; b_1, b_2, b_3 - coefficients for thermal conduction; α_L, α_H are dispersivity for mechanical and thermal dispersion; $S_{C\max}$ - interception storage capacity; K_C - canopy drainage rate; g_C - exponential decay parameter; and C_r - extinction coefficient of the vegetation for net radiation.

0.4, while for the night-time, C_r is calibrated to 0.08 to ensure the consistency of the predictions on both energy fluxes and soil temperature dynamics.

In unsaturated zone, the upper 1 m soil is defined as the computational area and discretized with a non-uniform mesh with 36 nodes. The topmost soil layer (0–8 cm) is discretized with a finer mesh with 1 cm to simulate the non-isothermal soil moisture transport under a steep gradient of capillary pressure and temperature. A larger mesh size of 2 cm is used for the depth between 8 and 32 cm. A relatively coarse mesh (4 cm) is used in the deeper soil profile (32–100 cm) where the soil temperature and moisture content are relatively less dynamic.

The results of the proposed model (non-isothermal multi-phase flow model integrated with land surface energy-balance equations) was compared with a simple model that coupled the Penman-Monteith equation with the Richards' equation (PM-RE model). The FAO Penman-Monteith equation is widely-used to determine the reference evaporation rate, a predefined ground heat flux was used to account the single-layer energy-balance (Allen et al., 1998). The Richards' equation (i.e., combining Eq. 15 and Eq. 21) used the same parameter set for soil hydraulic parameters (Table 3) and root water uptake (Eqs. 10–12), the impact of soil moisture stress on evaporation flux is included through Eq. A13. Note that the simple model can only simulate the total evaporation and isothermal soil moisture transport, but neglects the soil heat transport. The soil temperature, vapour transport in vadose zone, and the partitioned evaporation fluxes can only be simulated with proposed model.

RESULTS

Soil moisture

The measured soil moisture content in response to the rainfall is shown in Fig. 2. The multiple rain-pulses can be roughly separated into three main events. The first event occurs on DoY 217 with the rainfall intensity of 10 mm/h lasting two hours. During the second (DoY 233-243) and third (DoY 260-263) rain events the rainfall amount is 23 mm and 55 mm respectively. Under high-intensity rainfall, the soil moisture content of three depths dramatically increased to 0.5, then generally decreased to 0.2–0.3. The measured fast response of soil moisture may be caused by the occurrence of preferential flow, while its influence on infiltration might only last for a few hours (Figs. 2b–c). The propagation of wetting fronts was attenuated, because a fraction of infiltrated rainwater was stored in the upper-layer soil (i.e., 0–8 cm). Consequently, less rainwater can infiltrate to the deeper soil (e.g., 64 cm depth).

The simulated soil moisture content by the proposed non-isothermal model and the simple PM-RE model at three different depths (8 cm, 32 cm, and 64 cm) is also shown in Fig. 2, and their RMSE and bias compared with the measurement during the calibration and validation periods are listed in Table 4. Under high-intensity rainfall, the response of simulated soil moisture content of both two models in deeper soil (32 and 64 cm) shows time delay to rainfall pulses, and the simulated peak moisture content is under-estimated. In dry-down periods, the moisture content decreased gradually. The simple model overestimated the soil moisture content, the simulated moisture content by non-isothermal model gives a good match with the measurement. The error statistics indicates all RMSEs and absolute values of bias of soil moistures of non-isothermal model at three different depths are less than 0.05 and 0.01 respectively (Table 4).

Soil temperature

Simulated by the proposed non-isothermal model, the measured and simulated soil temperature at four different depths (4 cm, 8 cm, 32 cm, and 64 cm) are shown in Fig. 3. The RMSE and bias during the calibration and validation periods are listed in Table 4. Both the ground heat flux and the soil temperature have clear diurnal periodic patterns as shown in Fig. 3. Additionally, the amplitudes of soil temperature were decreasing along with the increasing depth of soil profile. Specifically, the average diurnal amplitude of soil temperature at 4 cm depth is approximately 10°C, while the amplitudes at 8 and 32 cm are approximately 5°C and 2°C, respectively. The soil temperature at 64 cm depth did not show a significant diurnal pattern, and its amplitude is even lower than 1°C (Fig. 3).

The amplitude of soil temperature is also affected by rainfall-infiltration that increases both soil moisture and soil heat capacity. For example, the amplitude of ground heat flux and soil temperature during the second rainfall period (e.g., DoY 233-243) are relatively small as the net radiation and atmosphere temperature were lower than that during the intermittent period.

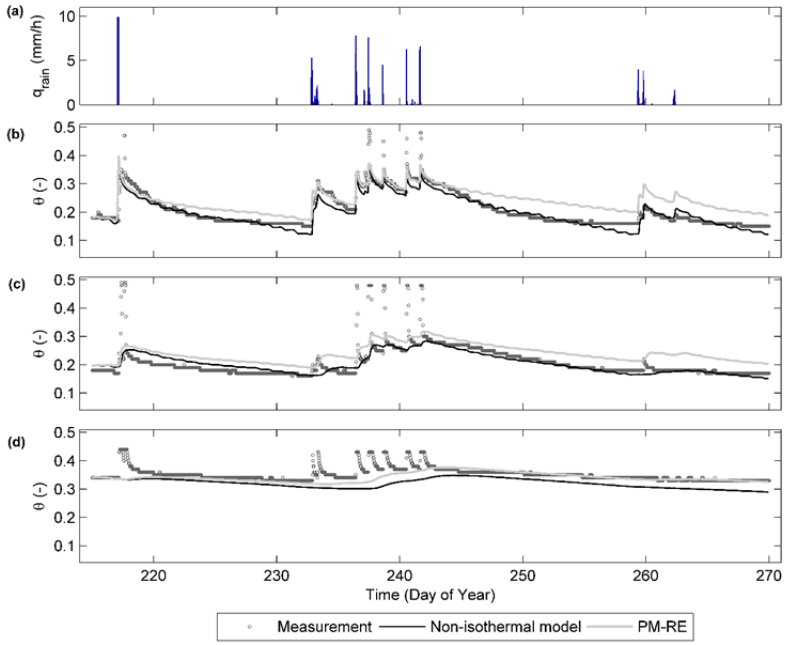

Fig. 2. (a) Measured rainfall intensity (bar), and measured soil water content at the depths of (b) 8 cm, (c) 32 cm, and (d) 64 cm below the ground surface over the study period of DoY 215-DoY 270 in 2004. The soil moisture content at different depths simulated by the simple model and by the proposed non-isothermal model are given as grey line and black line, respectively.

Table 4. Comparisons of the RMSE and bias between measurements and simulations from the proposed non-isothermal model in terms of soil moisture content (–) and soil temperature (°C) at the depth of 4, 8, 32, and 64 cm below the surface for both calibration and validation periods, respectively. Comparisons of the RMSE and bias between measurements and the simulated soil moisture content from the simple model (i.e., Penman-Monteith equation coupled with Richards's Equation) are given in the bracket, note that the simple model can only simulate soil moisture content but cannot simulate soil temperature.

	Soil moisture content (–)				Soil temperature (°C)			
Depth	Calibration		Validation		Calibration		Validation	
(cm)	RMSE	Bias	RMSE	Bias	RMSE	Bias	RMSE	Bias
4	–	–	–	–	1.41	–0.17	1.75	–0.62
8	0.022 (0.030)	–0.008 (0.017)	0.020 (0.049)	–0.004 (0.039)	1.02	0.03	1.30	–0.33
32	0.034 (0.043)	–0.002 (0.031)	0.038 (0.050)	–0.010 (0.032)	0.79	–0.02	0.84	–0.21
64	0.033 (0.027)	–0.002 (–0.016)	0.041 (0.023)	–0.004 (–0.007)	1.03	0.66	0.85	0.58

The errors at different depths are provided in Table 4. Compared with the measurements, the RMSE of simulated soil temperature is 1.75°C, while the bias is relatively small with an absolute value less than 1°C. Relatively large RMSEs of topmost soil temperature at 4 cm depth indicate that the amplitude of diurnal variation was slightly underestimated. On the contrary, the RMSE and bias of soil temperature at deeper soil (8, 32, and 64 cm) show that both of amplitude and daily averaged values of soil temperature are well simulated.

Vapour transport in soil

The vapour transport in vadose zone can be simulated with the proposed multi-phase flow model, and the equivalent energy flux of vapour flow during a 7-day period is shown in Figure 4. The vapour flow transports at depths of 0, 1, 10, and 20 cm show clear diurnal patterns (Fig. 4). In particular, at the surface (0 cm), the vapour flux rate reaches a maximum value of 2.2 W m^{-2} around noon (i.e., at 12 h), and then reduces to about zero at night. However, the vapour flow at deeper depths demonstrates of the opposite diurnal pattern - the vapour flow in deeper soil is downward after the noon, but upward at night. The drying front is not obvious in the study site, indicating that the evaporation is mainly from soil surface under such relatively wet condition. The amplitude of the vapour flow is decreasing from around 6 W m^{-2} (at 1 cm) to 2 W m^{-2} (at 20 cm) (Fig. 4).

Energy fluxes

The averaged diurnal cycle of measured net radiation during both of calibration and validation periods was analysed (Fig. 5). The averaged net radiation significantly increases after 6 h in the morning from below 0 W m^{-2}, reaching its maximum value of around 600 W m^{-2} in the noon (i.e., at 12 h). Then the net radiation starts to decrease and generally approaching zero. During the night, the net radiation is below 0 W m^{-2}, because the upward infrared radiation may be larger than the downward infrared radiation. The sensible heat and latent heat show similar averaged diurnal cycles compared with the net radiation (an increase from 6 h, peak around 12 h, and bottom around 18 h), except for the amplitudes. The average daily sensible heat is fluctuated from below 0 W m^{-2} (during the night) to around 400 W m^{-2} (at noon), while the average daily latent heat is ranged from around 0 W m^{-2} (during the night) to around 200 W m^{-2} (at noon).

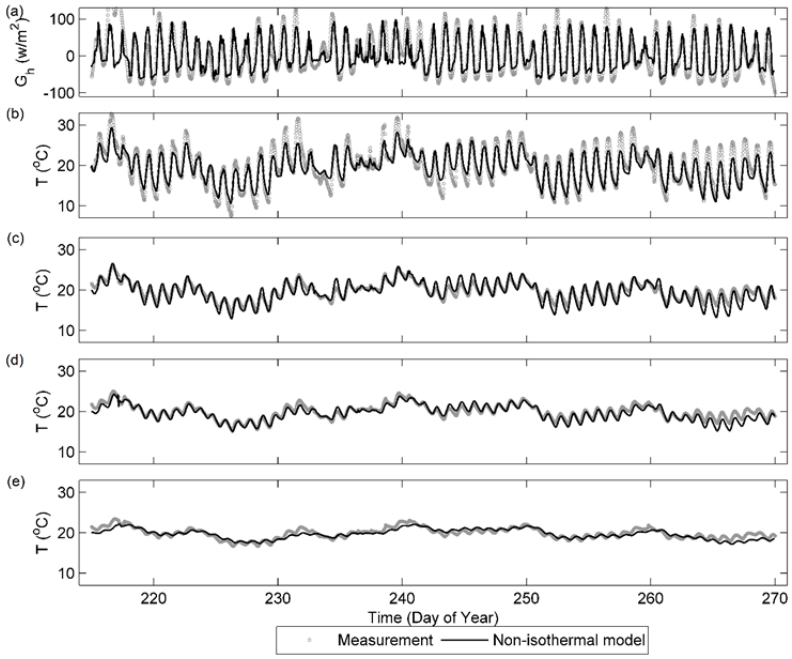

Fig. 3. Simulated and measured (a) ground heat fluxes, and soil temperature at four different depths of (b) 4 cm, (c) 8 cm, (d) 32 cm, and (e) 64 cm over the study period of DoY 215-DoY270 in 2004.

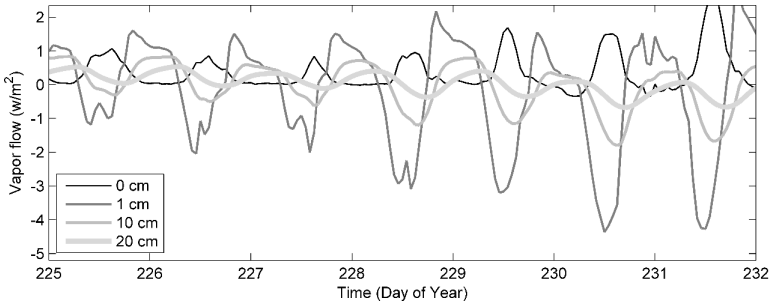

Fig. 4. The equivalent energy flux of vapour transport λq_v at depths of 0 cm, 1 cm, 10 cm, and 20 cm during a 7-day period. The vapour flux of advection, diffusion and dispersion q_v is expressed as $q_v = \rho_v q_a + \theta_a J_v$. Positive values represent the upward vapour flow.

During both the calibration and validation periods, the deviations between the simulated and measured ground heat and sensible heat fluxes shown in Fig. 5 might correspond to the simplification of radiative transfer algorithm (Eq. 1, 2), which neglects the impact of canopy structure (e.g., leaf angle distribution, vertical distribution of leaf area) on radiation transfer. The overall performance of the simulated sensible heat, latent heat, and ground heat fluxes are satisfying compared with measurements during both calibration and validation periods, giving within 22 W m^{-2} of RMSEs and within ±7 W m^{-2} of biases (Table 5).

Table 5. Comparisons of RMSE and bias between simulations and measurements of sensible heat, latent heat, and ground heat for both calibration and validation periods, respectively. Unit: W/m^2.

Energy flux	Calibration		Validation	
	RMSE	Bias	RMSE	Bias
λE	21.3	–4.2	19.0	1.2
H	15.4	2.2	16.4	–6.7
G_H	18.4	2.4	20.5	–5.7

Evaporation rates

The potential evaporation rate simulated by the FAO Penman-Monteith equation gives a good fit to the measured values (RMSE = 0.64 mm, bias = –0.29 mm). However, the actual evaporation simulated by the simple model using the FAO Penman-Monteith equation coupled with the Richards' equation are underestimated compared with the measurement (RMSE = 1.06 mm, bias = –0.74 mm). On the contrary, the total evaporation calculated by the proposed model is much more accurate compared to the simple model. The RMSE of the proposed model is 0.77 mm, while the bias is only 0.17 mm.

The simulated three components of evaporation fluxes using the proposed model are shown in Fig. 6. The study area was nearly fully-covered by forest canopy, and the transpiration dominated the total evaporation as expected. Based on the simulated evaporation fluxes, 86% of total evaporation was from transpiration, only 11% of total evaporation was from the soil surface, and the remaining 3% evaporation was from interception (Fig. 6). After the rainfall, the total evaporation generally reached to a peak rate of 6.5 mm day^{-1} (e.g., DoY 218-219), while it was generally decreasing as the soil getting dryer (DoY 220-227 and DoY 263-270). The soil surface evaporation had a similar pattern but with a relative small fluctuation, especially when the moisture content in the topmost soil is lower than 0.20 (DoY 255-260). The interception evaporation occurred only during or after rainfall.

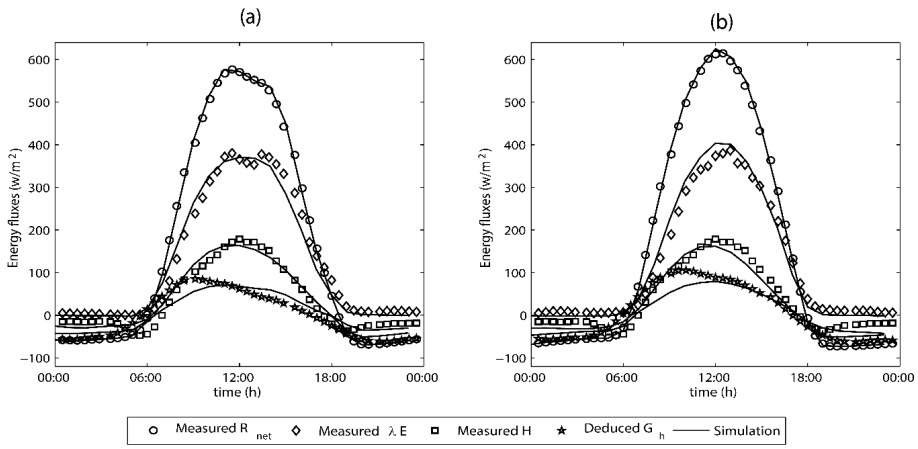

Fig. 5. The averaged diurnal cycle of the energy fluxes of net radiation (circles), sensible heat (diamonds), latent heat (squares), ground heat fluxes (stars), and simulations (solid lines) during (a) calibration period, and (b) validation period. The energy fluxes are calculated by Equation 3 and 4 (for detail see Table 1 and Appendix).

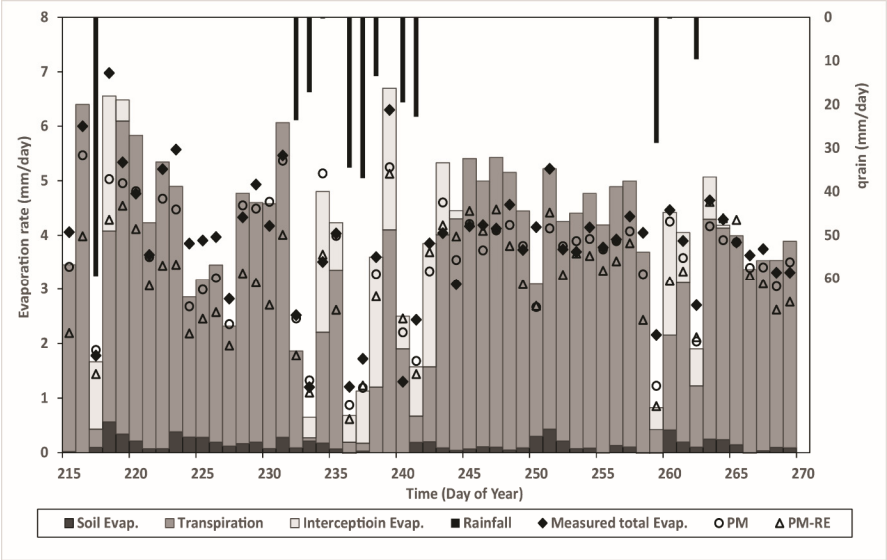

Fig. 6. Measured total evaporation, calculated potential evaporation by FAO Penman-Monteith equation (FAO-PM), calculated actual evaporation by the simple model (PM-RE: Penman-Monteith equation coupled with Richards' equation), and simulated fluxes of three evaporation components by the proposed model (energy-balance equations coupled with non-isothermal soil moisture transport).

DISCUSSION

In a hydrological system, evaporation is an important process that affects both water balance and energy balance. Specifically, the energy fluxes are strongly coupled with the soil system: the variations of soil surface temperature can affect both sensible heat and ground heat flux, and the soil moisture in topsoil and root zone can impact soil surface evaporation and transpiration respectively (Saito et al., 2006). A recently study by Garcia Gonzalez et al., (2012) indicated that the simulated soil surface temperature and evaporation fluxes may be deviating from reality because of using a simplified soil heat and water flow equation. The quantification and prediction of evaporation fluxes still have large uncertainties, especially when the complex physical processes are not adequately represented by the modelling system (Coenders-Gerrits et al., 2014).

The model proposed and applied in this study is focused on improving the representation of soil moisture and energy transport processes within an SVAT system, which may potentially give more realist simulations of land-atmosphere interaction. The case study was conducted for a deciduous broadleaf forest area with well-instrumented measurements, and the physiological behaviour of leaf stomata in the typical oak forest area can be parameterized based on previous literature (Baldocchi et al., 1987). Only the soil hydraulic parameters and extinction coefficients were calibrated.

Integrating the soil thermal transport with a two-layer energy-balance method in a SVAT model can assist in calibrating the extinction coefficient C_r. The ground heat flux is interacted with the diurnal variation of soil temperature, despite the fact that the contribution of soil evaporation to total evaporation is relatively small. For example, an over-estimation of C_r will lead to an underestimation of the ground heat flux, consequently, amplitude and values of the soil temperature may also be underestimated. Coupling of soil thermal transport with energy-balance model may bring a more reliable estimation of ground heat flux.

The simulated total evaporation flux was compared with a simple model that couples Penman–Monteith model with the Richards' equation. The simple model underestimated the total evaporation rate, which might be related to the following reasons. The Penman–Monteith equation used a pre-defined ground heat flux that may affect the accuracy of calculated energy fluxes. The Penman–Monteith equation simulates a reference evaporation rate, the multiply environmental stress on

transpiration rate is considered for grassland. The oak forest species may show different physiological behaviour in response to solar radiation, temperature, and soil moisture stress, which could all affect the transpiration rate.

In forest area, the liquid water transport can be affected by both preferential flow and matrix flow. Previous studies (e.g., Dusek et al., 2008; Shao et al., 2015, 2016) indicated that the preferential flow through macropores, and other local high permeability zones may be extremely rapid and instantly affect the hydrological response. The results in this study indicate that the peak soil moisture content during the rainy period was underestimated if neglecting the impact of preferential flow, even though the proposed model can adequately simulate the soil moisture content in root zone during the intermittent period (when no rainfall occurs). The soil moisture stored in matrix has relatively low flow velocity and long residence time, which is more correlated with the evaporation fluxes. Moreover, the matrix flow can cause exfiltration delivering water upward to the topmost soil for sustaining soil surface evaporation. However, for simulating the groundwater percolation and stream flow generation processes, the incorporation of preferential flow processes in modelling systems is still essential.

CONCLUSIONS

A multiphase flow model was coupled with a two-layer energy-balance model to simulate both energy and moisture fluxes in a soil-vegetation-atmosphere continuum. The model was applied using data of an experimental Oak-hickory forest area in Missouri, USA, covering 55 days during the late-summer period. The measurements of soil and vegetation information were used to parameterize the model. The model was driven by meteorological forcing data of net radiation, atmosphere temperature, air humidity and wind speed. The measured energy fluxes and soil temperature and moisture were used to calibrate and validate the model.

The simulated results of energy fluxes, soil moisture and temperature were in good agreements with the measured values, showing a satisfying model simulating ability. In comparison with the simple model coupling Penman-Monteith equation with Richards' equation, the proposed model provided a better estimation of total evaporation rate and meanwhile it could partition the evaporation into interception, soil evaporation and transpiration. In such forest area with a dense canopy cover, 86% of total evaporation is from transpiration, the interception accounts for 3%, and only 11% of total evaporation is from the soil surface. The results indicate that the proposed model can simulate the total evaporation rate and soil moisture/temperature, which may be a promising tool to provide more detailed simulations of energy and moisture fluxes in a soil-vegetation-atmosphere continuum.

*Acknowledgements.*The research was supported by the EU COST Action 1306 project LD15130 "Impact of landscape disturbance on the stream and basin connectivity". Wei Shao would like to acknowledge the financial support from research grant (HKUST6/CRF/12R) provided by the Research Grants Council of the Government of the Hong Kong. We thank Dr. Miriam Coenders-Gerrits (Water Resources Department, Delft University of Technology) and Dr. Yijian Zeng (ITC Faculty, University of Twente) for critical comments which help us to improve the quality of the paper. The helpful and constructive comments and suggestions from the anonymous reviewers are appreciated.

REFERENCES

Allen, R.G., Pereira, L.S., Raes, D., Smith, M., 1998. Crop evapotranspiration-guidelines for computing crop water requirements. FAO Irrigation and Drainage Paper, No. 56, Rome, 210 p.

Baldocchi, D.D., Hicks, B.B., Camara, P., 1987. A canopy stomatal resistance model for gaseous deposition to vegetated surfaces. Atmos. Environ., 21, 1, 91–101. DOI: 10.1016/0004-6981(87)90274-5.

Bonan, G.B., Williams, M., Fisher, R.A., Oleson, K.W., 2014. Modeling stomatal conductance in the earth system: linking leaf water-use efficiency and water transport along the soil-plant-atmosphere continuum. Geosci. Model Dev., 7, 5, 2193–2222. DOI:10.5194/gmd-7-2193-2014.

Celia, M.A., Bouloutas, E.T., Zarba, R.L., 1990. A general mass-conservative numerical solution for the unsaturated flow equation. Water Resour. Res., 26, 7, 1483–1496. DOI:10.1029/WR026i007p01483.

Choudhury, B.J., Monteith, J.L., 1988. A four-layer model for the heat budget of homogeneous land surfaces. Q. J. R. Meteorol. Soc., 114, 480, 373–398. DOI:10.1002/qj.49711448006.

Chung, S.-O., Horton, R., 1987. Soil heat and water flow with a partial surface mulch. Water Resour. Res., 23, 12, 2175–2186. DOI:10.1029/WR023i012p02175.

Coenders-Gerrits, A.M.J., van der Ent, R.J., Bogaard, T.A., Wang-Erlandsson, L., Hrachowitz, M., Savenije, H.H.G., 2014. Uncertainties in transpiration estimates. Nature, 506, 7487, E1-E2. DOI:10.1038/nature12925.

Colaizzi, P.D., Kustas, W.P., Anderson, M.C., Agam, N., Tolk, J.A., Evett, S.R., Howell, T.A., Gowda, P.H., O'Shaughnessy, S.A., 2012. Two-source energy balance model estimates of evapotranspiration using component and composite surface temperatures. Adv.Water Resour., 50, 134–151. DOI: 10.1016/j.advwatres.2012.06.004.

Davarzani, H., Smits, K., Tolene, R.M., Illangasekare, T., 2014. Study of the effect of wind speed on evaporation from soil through integrated modeling of the atmospheric boundary layer and shallow subsurface. Water Resour. Res., 50, 1, 661–680. DOI:10.1002/2013wr013952.

Dohnal, M., Černý, T., Votrubová, J., Tesař, M., 2014. Rainfall interception and spatial variability of throughfall in spruce stand. J. Hydrol. Hydromech., 62, 277–284.

Dusek, J., Gerke, H.H., Vogel, T., 2008. Surface boundary conditions in 2D dual-permeability modeling of tile drain bromide leaching. Vadose Zone J., 7, 1287–1301. DOI: 10.2136/vzj2007.0175.

Eltahir, E., Bras, R., 1993. A description of rainfall interception over large areas. J. Clim., 6, 6, 1002–1008.

Eltahir, E.A.B., 1998. A soil moisture-rainfall feedback mechanism: 1. Theory and observations. Water Resour. Res., 34, 4, 765–776. DOI:10.1029/97WR03499.

Entekhabi, D., Rodriguez-Iturbe, I., Castelli, F., 1996. Mutual interaction of soil moisture state and atmospheric processes. J. Hydrol., 184, 1–2, 3–17. DOI: 10.1016/0022-1694(95)02965-6.

Feddes, R.A., Hoff, H., Bruen, M., Dawson, T., de Rosnay, P., Dirmeyer, P., Pitman, A.J., 2001. Modeling root water uptake in hydrological and climate models. Bull. Am. Meteorol. Soc., 82, 12, 2797–2809.

Garcia Gonzalez, R., Verhoef, A., Luigi Vidale, P., Braud, I., 2012. Incorporation of water vapor transfer in the JULES land surface model: Implications for key soil variables and land surface fluxes. Water Resour. Res., 48, 5, W05538. DOI:10.1029/2011WR011811.

Gerrits, A., Savenije, H., Veling, E., Pfister, L., 2009. Analytical derivation of the Budyko curve based on rainfall characteristics and a simple evaporation model. Water Resour. Res., 45, 4, W04403. DOI: 10.1029/2008WR007308.

Gran, M., Carrera, J., Olivella, S., Saaltink, M.W., 2011. Modeling evaporation processes in a saline soil from saturation to oven dry conditions. Hydrol. Earth Syst. Sci., 15, 7, 2077–2089. DOI:10.5194/hess-15-2077-2011.

Grifoll, J., 2013. Contribution of mechanical dispersion of vapor to soil evaporation. Water Resour. Res., 49, 2, 1099–1106. DOI:10.1002/wrcr.20105.

Grifoll, J., Gastó, J.M., Cohen, Y., 2005. Non-isothermal soil water transport and evaporation. Adv. Water Resour., 28, 11, 1254–1266. DOI: 10.1016/j.advwatres.2005.04.008.

Guimberteau, M., Ducharne, A., Ciais, P., Boisier, J.P., Peng, S., De Weirdt, M., Verbeeck, H., 2014. Testing conceptual and physically based soil hydrology schemes against observations for the Amazon Basin. Geosci. Model Dev., 7, 3, 1115–1136. DOI:10.5194/gmd-7-1115-2014.

Ivanov, V.Y., Bras, R.L., Vivoni, E.R., 2008. Vegetation-hydrology dynamics in complex terrain of semiarid areas: 1. A mechanistic approach to modeling dynamic feedbacks. Water Resour. Res., 44, 3, W03429. DOI:10.1029/2006wr005588.

Jarvis, P.G., 1976. The interpretation of the variations in leaf water potential and stomatal conductance found in canopies in the field. Philosophical Transactions of the Royal Society of London. B, Biological Sciences, 273, 927, 593–610. DOI:10.1098/rstb.1976.0035.

Kollet, S.J., Maxwell, R.M., 2008. Capturing the influence of groundwater dynamics on land surface processes using an integrated, distributed watershed model. Water Resour. Res., 44, 2, W02402. DOI:10.1029/2007WR006004.

Milly, P.C.D., 1984. A simulation analysis of thermal effects on evaporation from soil. Water Resour. Res., 20, 8, 1087–1098. DOI:10.1029/WR020i008p01087.

Mosthaf, K., Baber, K., Flemisch, B., Helmig, R., Leijnse, A., Rybak, I., Wohlmuth, B., 2011. A coupling concept for two-phase compositional porous-medium and single-phase compositional free flow. Water Resour. Res., 47, 10, W10522. DOI:10.1029/2011wr010685.

Overgaard, J., Rosbjerg, D., Butts, M.B., 2006. Land-surface modelling in hydrological perspective – a review. Biogeosciences, 3, 2, 229–241. DOI:10.5194/bg-3-229-2006.

Parlange, M.B., Cahill, A.T., Nielsen, D.R., Hopmans, J.W., Wendroth, O., 1998. Review of heat and water movement in field soils. Soil and Tillage Research, 47, 1–2, 5–10. DOI: 10.1016/S0167-1987(98)00066-X.

Pinder, G.F., Celia, M.A., 2006. Subsurface Hydrology. John Wiley & Sons, 484 p.

Rodriguez-Iturbe, I., 2000. Ecohydrology: A hydrologic perspective of climate-soil-vegetation dynamies. Water Resour. Res., 36, 1, 3–9. DOI:10.1029/1999WR900210.

Rutter, A.J., Kershaw, K.A., Robins, P.C., Morton, A.J., 1971. A predictive model of rainfall interception in forests. 1. Derivation of the model from observations in a plantation of Corsican pine. Agric. Meteorol., 9, 367–384, DOI: 10.1016/0002-1571(71)90034-3.

Saito, H., Šimůnek, J., Mohanty, B.P., 2006. Numerical analysis of coupled water, vapor, and heat transport in the vadose zone. Vadose Zone J., 5, 2, 784–800. DOI:10.2136/vzj2006.0007.

Sakai, M., Jones, S.B. Tuller, M., 2011. Numerical evaluation of subsurface soil water evaporation derived from sensible heat balance. Water Resour. Res., 47, 2, W02547. DOI: 10.1029/2010WR009866.

Savenije, H.H.G., 2004. The importance of interception and why we should delete the term evapotranspiration from our vocabulary. Hydrol. Process., 18, 8, 1507–1511. DOI:10.1002/hyp.5563.

Seneviratne, S.I., Corti, T., Davin, E.L., Hirschi, M., Jaeger, E.B., Lehner, I., Orlowsky, B., Teuling, A.J., 2010. Investigating soil moisture–climate interactions in a changing climate: A review. Earth-Sci. Rev., 99, 3–4, 125–161. DOI: 10.1016/j.earscirev.2010.02.004.

Shao, W., Bogaard, T. A., Bakker, M., Greco, R., 2015. Quantification of the influence of preferential flow on slope stability using a numerical modelling approach. Hydrol. Earth Syst. Sci., 19, 5, 2197–2212. DOI:10.5194/hess-19-2197-2015.

Shao, W., Bogaard, T. A., Bakker, M., Berti, M., 2016. The influence of preferential flow on pressure propagation and landslide triggering of the Rocca Pitigliana landslide. J. Hydrol., 543(B), 360–372. DOI: 10.1016/j.jhydrol.2016.10.015.

Šimůnek, J., Sejna, M., Saito, H., Sakai, M., van Genuchten, M.T., 2013. The HYDRUS-1D software package for simulating the one-dimensional movement of water, heat, and multiple solutes in variably-saturated media, version 4.17. Department of Environmental Sciences, University of California Riverside, Riverside, California, USA, 242 p.

Šír, M., Syrovátka, O., Pražák, J., Lichner, Ľ., 2001. Soil water regime in head water regions-observation, assessment and modelling. J. Hydrol. Hydromech., 49, 355–375.

Smits, K.M., Cihan, A., Sakaki, T., Illangasekare, T.H., 2011. Evaporation from soils under thermal boundary conditions: Experimental and modeling investigation to compare equilibrium- and nonequilibrium-based approaches. Water Resour. Res., 47, 5, W05540. DOI:10.1029/2010wr009533.

Smits, K.M., Ngo, V.V., Cihan, A., Sakaki, T., Illangasekare, T.H., 2012. An evaluation of models of bare soil evaporation formulated with different land surface boundary conditions and assumptions. Water Resour. Res., 48, 12, W12526. DOI:10.1029/2012wr012113.

Stewart, J.B., 1988. Modelling surface conductance of pine forest. Agric. For. Meteorol., 43, 1, 19–35. DOI: 10.1016/0168-1923(88)90003-2.

van de Griend, A.A., Owe, M., 1994. Bare soil surface resistance to evaporation by vapor diffusion under semiarid conditions. Water Resour. Res., 30, 2, 181–188. DOI:10.1029/93wr02747.

van Dijk, A.I.J.M., Bruijnzeel, L.A., 2001. Modelling rainfall interception by vegetation of variable density using an adapted analytical model. Part 1. Model description. J. Hydrol., 247, 3–4, 230–238. DOI: 10.1016/S0022-1694(01)00392-4.

van Genuchten, M.T., 1980. A closed-form equation for predicting the hydraulic conductivity of unsaturated soils. Soil Sci. Soc. Am. J., 44, 5, 892–898.

van Genuchten, M.T., Leij, F., Yates, S., 1991. The RETC code for quantifying the hydraulic functions of unsaturated soils. Robert S. Kerr Environmental Research Laboratory.

Varado, N., Braud, I., Ross, P.J., 2006. Development and assessment of an efficient vadose zone module solving the 1D Richards' equation and including root extraction by plants. J. Hydrol., 323, 1–4, 258–275. DOI: 10.1016/j.jhydrol.2005.09.015.

Were, A., Villagarcía, L., Domingo, F., Moro, M.J., Dolman, A.J., 2008. Aggregating spatial heterogeneity in a bush vegetation patch in semi-arid SE Spain: A multi-layer model versus a single-layer model. J. Hydrol., 349, 1–2, 156–167. DOI: 10.1016/j.jhydrol.2007.10.033.

Xin, X., Liu, Q., 2010. The Two-layer Surface Energy Balance Parameterization Scheme (TSEBPS) for estimation of land surface heat fluxes. Hydrol. Earth Syst. Sci., 14, 3, 491–504. DOI:10.5194/hess-14-491-2010.

Yin, Z., Dekker, S.C., van den Hurk, B.J.J.M., Dijkstra, H.A., 2014. Effects of vegetation structure on biomass accumulation in a Balanced Optimality Structure Vegetation Model (BOSVM v1.0). Geosci. Model Dev., 7, 3, 821–845. DOI:10.5194/gmd-7-821-2014.

Zeng, Y., Su, Z., Wan, L., Wen, J., 2011. A simulation analysis of the advective effect on evaporation using a two-phase heat and mass flow model. Water Resour. Res., 47, 10, W10529. DOI:10.1029/2011wr010701.

Zhou, M.C., Ishidaira, H., Hapuarachchi, H.P., Magome, J., Kiem, A.S., Takeuchi, K., 2006. Estimating potential evapotranspiration using Shuttleworth–Wallace model and NOAA-AVHRR NDVI data to feed a distributed hydrological model over the Mekong River basin. J. Hydrol., 327, 1–2, 151–173. DOI: 10.1016/j.jhydrol.2005.11.013.

Received 20 April 2016
Accepted 11 February 2017

APPENDIX
Parameterization of resistance coefficients

The parameterization of the resistance coefficients is needed to calculate the energy fluxes using the equations from Table 1. The r_a is the aerodynamic resistance dictating the sensible heat flux between atmosphere and canopy layer (Choudhury and Monteith, 1988):

$$r_a = \frac{1}{k_{kar} u^*} \ln\left[\left(z_{ref} - d_{\mathrm{M}}\right)/z_0\right](1+\delta)^{\eta} \quad \text{(A1)}$$

where k_{kar} (=0.41) is Karman constant, η and δ are coefficients for stability correction based on Monin-Obukhov theories (Choudhury et al., 1986), and u^* (m/s) is the friction velocity:

$$u^* = \frac{k_{kar} u_{wind}}{\ln\left[\left(z_{ref} - d_M\right)/z_0\right]} \quad \text{(A2)}$$

where z_{ref} $(= h_{veg} + 2)$ is the reference height can be defined as 2 meters above the height of the vegetation canopy h_{veg}, g (9.81 m s^{-2}) is the gravitational acceleration; u_{wind} (m s^{-1}) is the wind speed at reference height. The zero displacement height d_M (m) and the roughness length for momentum z_0 (m) are determined following Choudhury and Monteith (1988):

$$d_M = 1.1 \times h_{veg} \ln\left[1 + \zeta_d^{0.25}\right] \quad \text{(A3)}$$

$$z_0 = \begin{cases} z_{0g} + 0.3 h_{veg} \zeta_d^{0.5} & 0 < \zeta_d < 0.2 \\ 0.3 h_{veg}\left(1 - d_M / h_{veg}\right) & 0.2 < \zeta_d < 1.5 \end{cases} \quad \text{(A4)}$$

where z_{0g} (m) is the roughness of soil surface with value of 0.02 m adopted in this study, ζ_d is the effective drag coefficient with a typical value of 0.2 for forest area.

The aerodynamic resistance to heat and water transfer in canopy layer is calculated by:

$$r_{ac} = \frac{\sigma_c}{I_{\mathrm{LAI}}} \frac{100}{n_e} \left(\frac{w_L}{u_{hc}}\right)^{0.5} \left[1 - \exp\left(-n_e/2\right)\right]^{-1} \quad \text{(A5)}$$

where σ_c (= 0.5) is the shielding factor, w_L is the characteristic leaf width with a typical value of 0.2 m for broadleaf forest (Monteith and Unsworth, 2013), n_e (–) is the eddy diffusivity decay constant that may be set to 4.25 for forest area (Zhou et al., 2006).

The aerodynamic resistance between soil surface and canopy layer is calculated by (Shuttleworth and Gurney, 1990):

$$r_{as} = \frac{h_{veg} \exp(n_e)}{n_e K_{edc}} \left[\exp\left(-\frac{n_e z_{0g}}{h_{veg}}\right) - \exp\left(-\frac{n_e\left(z_0 + d_M\right)}{h_{veg}}\right)\right] \quad \text{(A6)}$$

where K_{edc} is the eddy diffusivity decay constant:

$$K_{edc} = k_{kar} u^* \left(h_{veg} - d_{\mathrm{M}}\right) \quad \text{(A7)}$$

Soil surface resistance is formulated as an exponential function which links the evaporation process with the soil moisture condition (van de Griend and Owe, 1994):

$$r_S = 10 \exp\left[\alpha_\theta\left(\theta_{\min} - \theta_{top}\right)\right] \quad \text{(A8)}$$

where α_θ (–) is a fitting parameter with a recommended value of 35.63 (van de Griend and Owe, 1994); $\theta_{\min}$ is the empirical minimum value of 0.15 below which the evaporation rate is limited by soil moisture. θ_{top} (–) is the moisture content at1cm depth.

The transpiration rate is partly governed by the canopy structure and leaf morphology for absorbing radiation energy, partly governed by the physiology of stomatal in response to solar radiation, temperature, and humidity in the atmosphere and soil moisture stress. The parameterization for bulk stomatal resistance is formulated by the Jarvis-Stewart model to introduce the dynamic interaction between transpiration and environmental stress (Jarvis, 1976; Stewart, 1988):

$$r_c = \frac{r_{c,\,opt}}{I_{\mathrm{LAI}} \prod_i F_i(\mathrm{x})} \quad \text{(A9)}$$

where, $r_{c,\,opt}$ is the minimum value of stomatal resistance under optima environment, and its value for oak forest is 145 s m^{-1}. The $\prod_i F_i(\mathrm{x})$ is an empirical multiplicative stress function based on the observed response of transpiration rate to the multiple environmental stresses. In this study, four response functions are used to quantify the influence of radiation, vapour pressure deficit, leaf temperature, and soil moisture content on transpiration rate (Baldocchi et al.,1987; Zhou et al., 2006):

$$F_1(\mathbf{I}^{\downarrow}) = \frac{\mathbf{I}^{\downarrow}}{\mathbf{I}^{\downarrow} + B} \quad \text{(A10)}$$

$$F_2(D_{can}) = 1 - b_{vpd} D_{can} \quad \text{(A11)}$$

$$F_3(T_{veg}) = \frac{T - T_{\min}}{T_{opt} - T_{\min}} \left(\frac{T_{\max} - T}{T_{\max} - T_{opt}}\right)^{\left(\frac{T_{\max} - T_{opt}}{T_{opt} - T_{\min}}\right)} \quad \text{(A12)}$$

$$F_4(\theta_{avg}) = \begin{cases} 1, & \theta_{avg} \geq \theta_{field} \\ \dfrac{\theta_{avg} - \theta_{wilting}}{\theta_{field} - \theta_{wilting}}, & \theta_{field} < \theta_{avg} < \theta_{wilting} \\ 0, & \theta_{avg} \leq \theta_{wilting} \end{cases} \quad \text{(A13)}$$

where $F_1(\mathbf{I}^{\downarrow})$ is the hyperbolic radiation response function of photosynthetically active radiation $\mathbf{I}^{\downarrow}$ (w/m^2), B is the a curvature coefficient with a value of 22 w/m^2 for oak forest area (Baldocchi et al., 1987). $F_2(D_{can})$ is a linear equation quantifying the decreasing of transpiration rate with the vapour deficit D_{can} increasing, b_{vpd} is the shape coefficient with a value of 0 for oak forest (Baldocchi et al., 1987). Function $F_3(T_{veg})$ quantifies the influence of foliage temperature on transpiration, the T_{opt} is the optimum temperature, $T_{\min}$ and $T_{\max}$ are temperatures on which the transpiration is limited. The values of $T_{\min}$, T_{opt}, and $T_{\max}$ in oak forest area are 10, 28, and 45°C, respectively. $F_4(\theta_{avg})$ quantifies the impact of soil moisture stress on transpiration (Zhou et al., 2006), where θ_{avg} is the average moisture content in root zone, θ_{field} is the field capacity below which the plant transpires at less than its maximum value, and $\theta_{wilting}$ is the willing point below which the plant transpires stops. θ_{field} and $\theta_{wilting}$ are moisture content at field capacity and wilting point corresponding the pore water pressure head of –3.3 m and –150 m respectively.

SUPPLEMENTARY MATERIAL

Part A. Algorithms for solving of two-layer energy-balance equations

The sensible heat fluxes can be expressed as follows:

$$H = \rho_a c_p \frac{T_{can} - T_{atm}}{r_a} \tag{S1}$$

$$H_{can} = \rho_a c_p \frac{T_{veg} - T_{can}}{r_{ac}} \tag{S2}$$

$$H_{sur} = \rho_a c_p \frac{T_{sur} - T_{can}}{r_{as}} \tag{S3}$$

where T_{veg} and T_{sur} (K) are temperature of vegetation foliage and soil surface, T_{atm} and T_{can} (K) are atmosphere temperature at the reference height and at the canopy source height; r_a, r_{ac}, and r_{as} (s m^{-1}) are aerodynamic resistances between canopy and reference height, between foliage and canopy air, between soil surface and canopy air respectively; c_p (J kg^{-1} K^{-1}) is a specific heat capacity of moist air under a constant pressure, and ρ_a (kg m^{-3}) is density of the air.

The latent heat fluxes can be expressed as:

$$\lambda E = \frac{\rho_a c_p}{\gamma} \frac{e_{can} - e_{atm}}{r_a} \tag{S4}$$

$$\lambda E_{can} = \frac{\rho_a c_p}{\gamma} \frac{e^*_{veg} - e_{can}}{r_{ac} + r_c} \tag{S5}$$

$$\lambda E_{sur} = \frac{\rho_a c_p}{\gamma} \frac{e_{sur} - e_{can}}{r_{as} + r_s} \tag{S6}$$

where γ(Pa K^{-1}) is the psychometric constant; e^*_{veg} (Pa) is saturation vapour pressure of air in contact with vegetation foliage or soil surface, e_{can} and e_{atm} (Pa) are vapour pressure of atmosphere at the levels corresponding to vegetation canopy and reference height respectively, and e_{sur} is vapour pressure of the soil surface.

For solving the energy fluxes, we can obtain the following relations based on the Eqs. S1–S3 and Eqs. S4–S6:

$$g_a (T_{can} - T_{atm}) = g_1 (T_{veg} - T_{can}) + g_2 (T_{sur} - T_{can}) \tag{S7}$$

$$g_a (e_{can} - e_{atm}) = g_c (e^*_{veg} - e_{can}) + g_s (e_{sur} - e_{can}) \tag{S8}$$

with:

$$g_a = \frac{1}{r_a};\ g_1 = \frac{1}{r_{ac}};\ g_2 = \frac{1}{r_{as}};\ g_c = \frac{1}{r_{ac} + r_c};\ g_s = \frac{1}{r_{as} + r_s} \tag{S9}$$

The canopy temperature and canopy vapour pressure can be expressed as:

$$T_{can} = \frac{g_a T_{atm} + g_1 T_{veg} + g_2 T_{sur}}{g_a + g_1 + g_2} \tag{S10}$$

$$e_{can} = \frac{g_a e_{atm} + g_c e^*_{veg} + g_s e_{sur}}{g_a + g_c + g_s} \tag{S11}$$

Substitute equation S10 and S11 to the energy balance equation in the canopy layer:

$$\begin{aligned} R^{can}_{net} &= \lambda E_{can} + H_{can} \\ &= \frac{\rho_a c_p}{\gamma_{psy}} \frac{e^*_{veg} - e_{can}}{r_{ac} + r_c} + \rho_a c_p \frac{T_{veg} - T_{can}}{r_{ac}} \\ &= \frac{\rho_a c_p}{\gamma_{psy}} g_c \left(e^*_{veg} - \frac{g_a e_{atm} + g_c e^*_{veg} + g_s e_{sur}}{g_a + g_c + g_s} \right) \\ &+ \rho_a c_p g_1 \left(T_{veg} - \frac{g_a T_{atm} + g_1 T_{veg} + g_2 T_{sur}}{g_a + g_1 + g_2} \right) \\ &= \frac{\rho_a c_p}{\gamma_{psy}} \frac{g_c}{g_a + g_c + g_s} \left[e^*_{veg} (g_a + g_s) - g_a e_{atm} - g_s e_{sur} \right] \\ &+ \rho_a c_p \frac{g_1}{g_a + g_1 + g_2} \left[T_{veg} (g_a + g_2) - g_a T_{atm} - g_2 T_{sur} \right] \end{aligned} \tag{S12}$$

In Eq. S12, e_{atm} and T_{atm} are model input from meteorological forcing data; e_{sur} and T_{sur} are estimated from the vadose zone model. Moreover, e_{veg} and T_{veg} obey the following relation:

$$e^*_{veg} = 0.6108 \exp\left(\frac{17.27 T_{veg}}{T_{veg} + 237.3} \right) \tag{S13}$$

Therefore, substituting Eq. S13 to S12, we can obtain a nonlinear equation with only one unknown variable T_{veg}, which can be numerically solved using the Newton-Raphson algorithm.

Part B. Finite Difference Algorithms for non-isothermal soil moisture transport

B1. Water Flow equation (two conditions: Flux-Flux and Head-Flux)

The numerical scheme was applied considering the following discretized 1D geometry (Fig. S1):

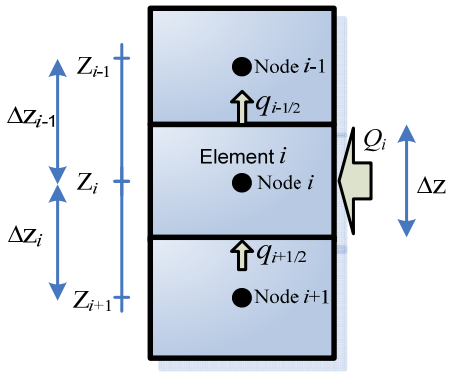

Fig. S1. Schematic representation of the mass balance derivation for middle nodes where

$$\Delta z = \frac{z_{i-1} - z_{i+1}}{2} \quad \Delta z_i = z_i - z_{i+1} \quad \Delta z_{i-1} = z_{i-1} - z_i \tag{S14}$$

The Richards' equation can be formulated by integrating the Darcy's Law with the water-balance equation:

$$C \frac{\partial h_w}{\partial t} = \frac{\partial}{\partial z} \left[K_w \left(\frac{\partial h_w}{\partial z} + 1 \right) \right] - Q \tag{S15}$$

where Q represent source/sink term and C is the differential water capacity:

$$C = \begin{cases} -\dfrac{d\theta}{d|h_w|} = m_{\mathrm{VG}} n_{\mathrm{VG}} \alpha_{\mathrm{VG}} (\theta_s - \theta_r) \Theta^{1/m_{\mathrm{VG}}} \left(1 - \Theta^{1/m_{\mathrm{VG}}}\right)^{m_{\mathrm{VG}}}, & h_w < 0 \\ S_S, & h_w \geq 0 \end{cases} \tag{S16}$$

where S_S is the specific storage of soils under fully saturated condition.

Equation S15 can be discretised with a fully-implicit finite difference method (Celia et al., 1990):

$$C_i^{n+1,\mathrm{m}} \frac{h_{c,i}^{n+1,\mathrm{m+1}} - h_{c,i}^{n+1,\mathrm{m}}}{\Delta t} + \frac{\theta_{w,i}^{n+1,\mathrm{m}} - \theta_{w,i}^{n}}{\Delta t} = \frac{1}{\Delta z}\left[K_{w,i-1/2}^{n+1,\mathrm{m}} \frac{(h_{w,i-1}^{n+1,\mathrm{m+1}} - h_{\mathrm{w},i}^{n+1,\mathrm{m+1}})}{\Delta z_{i-1}} - K_{w,i+1/2}^{n+1,m} \frac{(h_{w,i}^{n+1,\mathrm{m+1}} - h_{w,i+1}^{n+1,\mathrm{m+1}})}{\Delta z_i} \right] + \frac{K_{w,i-1/2}^{n+1,\mathrm{m}} - K_{w,i+1/2}^{n+1,\mathrm{m}}}{\Delta z} \cos\alpha - Q_i^{n+1,\mathrm{m}} \tag{S17}$$

where the superscript n is time level, and m is iteration level for solving the Richards' equation.

Rearranging the Eq. S17, we can get the following linearized equation:

$$a_i h_{w,i-1}^{n+1,\mathrm{m+1}} + b_i h_{w,i}^{n+1,\mathrm{m+1}} + c_i h_{w,i+1}^{n+1,\mathrm{m+1}} = e_i \tag{S18}$$

$$\begin{cases} a_i = -\dfrac{K_{w,i-1/2}^{n+1,\mathrm{m}}}{\Delta z_{i-1}} \\ b_i = \dfrac{\Delta z}{\Delta t} C_i^{n+1,\mathrm{m}} + \dfrac{K_{w,i-1/2}^{n+1,\mathrm{m}}}{\Delta z_{i-1}} + \dfrac{K_{w,i+1/2}^{n+1,\mathrm{m}}}{\Delta z_i} \\ c_i = -\dfrac{K_{w,i+1/2}^{n+1,\mathrm{m}}}{\Delta z_i} \qquad i = [1, Nz-1] \\ e_i = \dfrac{\Delta z}{\Delta t}\left[C_i^{n+1,\mathrm{m}} h_{\mathrm{w},i}^{n+1,\mathrm{m}} - \theta_{w,i}^{n+1,\mathrm{m}} + \theta_{w,i}^{n} \right] + \\ + \cos\alpha \left(K_{w,i-1/2}^{n+1,\mathrm{m}} - K_{w,i+1/2}^{n+1,\mathrm{m}} \right) - \Delta z \left(Q_i^{n+1,\mathrm{m}} \right) \end{cases} \tag{S19}$$

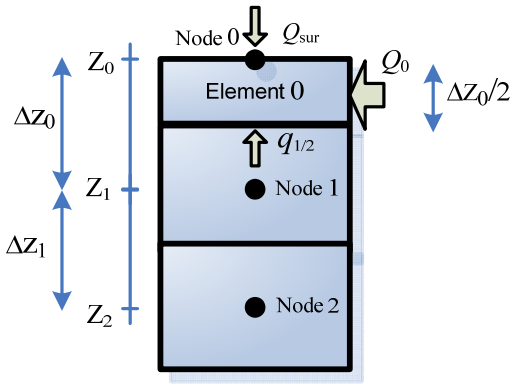

Fig. S2. Schematic representation of the mass balance derivation for top nodes.

(1) First type of boundary condition: pressure head boundary condition

The pressure head boundary condition suits to ponding infiltration condition. If the surface potential head is H_{sur}, the potential head of the first node of soil profile is $h_0 = H_{sur}$, thus, the first function is expressed as:

$$b_1 h_1^{n+1,m+1} + c_1 h_2^{n+1,m+1} = e_1 - a_1 H_{sur} \tag{S20}$$

If we set the bottom potential head as H_{bottom}, then the water head of the last node of soil profile is $h_{Nz} = H_{bottom}$, thus, the last function is expressed as:

$$a_{Nz-1} h_{Nz-2}^{n+1,m+1} + b_{Nz-1} h_{Nz-1}^{n+1,m+1} = e_{Nz-1} - c_{Nz-1} H_{bottom} \tag{S21}$$

(2) Second type of boundary condition: the flux boundary condition

A mass-conservative solution can be derived from the mass balance principle (Fig. S2):

$$\Delta t (Q_{sur} + q_{i+1/2} + Q_i^n \Delta z_0 / 2) = \left(\theta_i^{n+1} - \theta_i^n\right) \Delta z_0 / 2 \tag{S22}$$

Then we can use the Darcy's Law:

$$\frac{\theta_{w,0}^{n+1,p+1} - \theta_{w,0}^{n}}{\Delta t} = C_0^{n+1,\mathrm{m}} \frac{h_{\mathrm{w},0}^{n+1,\mathrm{m+1}} - h_{\mathrm{w},0}^{n+1,\mathrm{m}}}{\Delta t} + \frac{\theta_{w,0}^{n+1,\mathrm{m}} - \theta_{w,0}^{n}}{\Delta t} = 2 \frac{Q_{sur}^{n+1} - K_{1/2}^{n+1,m}\left(\dfrac{h_{w,0}^{n+1,m+1} - h_{w,1}^{n+1,m+1}}{\Delta z_0} + 1 \right)}{\Delta z_0} + Q_0^{n+1} \tag{S23}$$

Similarly, by rearranging the above-equation we can obtain:

$$\left(\frac{\Delta z_0}{2\Delta t} C_0^{n+1,m} + \frac{K_{w,1/2}^{n+1,m}}{\Delta z_0} \right) h_{w,0}^{n+1,m+1} - \frac{K_{w,1/2}^{n+1,m}}{\Delta z_0} h_{w,1}^{n+1,m+1} = \frac{\Delta z_0}{2\Delta t}\left[C_0^{n+1,m} h_{w,0}^{n} - \left(\theta_{w,0}^{n+1,m} - \theta_{w,0}^{n} \right) \right] + \left(Q_{sur}^{n+1} - K_{w,1/2}^{n+1,m} \right) + \frac{\Delta z_0}{2} Q_0^{n+1} \tag{S24}$$

Similarly, we can also derive this equation from the mass balance equation. If we control the bottom flux, the last function can be obtained by the following steps:

$$\frac{\partial \theta}{\partial t} + \frac{\partial q}{\partial z} = Q \tag{S25}$$

$$\frac{\theta_{Nz}^{n+1,m+1} - \theta_{Nz}^{n}}{\Delta t} = C_0^{n+1,\mathrm{m}} \frac{h_{\mathrm{w},Nz}^{n+1,\mathrm{m+1}} - h_{\mathrm{w},Nz}^{n+1,\mathrm{m}}}{\Delta t} + \frac{\theta_{w,Nz}^{n+1,\mathrm{m}} - \theta_{w,Nz}^{n}}{\Delta t} = 2 \frac{-q_{w,Nz-1/2}^{n+1,m+1} - Q_{bottom}^{n+1}}{\Delta z_{Nz-1}} + Q_{Nz}^{n+1} \tag{S26}$$

$$C_0^{n+1,\mathrm{m}}\frac{h_{\mathrm{w},Nz}^{n+1,\mathrm{m}+1}-h_{\mathrm{w},Nz}^{n+1,\mathrm{m}}}{\Delta t}+\frac{\theta_{w,Nz}^{n+1,\mathrm{m}}-\theta_{w,Nz}^{n}}{\Delta t}=2\frac{\left[K_{Nz-1/2}^{n+1,m}\left(\frac{h_{Nz-1}^{n+1,m+1}-h_{Nz}^{n+1,m+1}}{\Delta z_{Nz-1}}+1\right)\right]-Q_{bottom}^{n+1}}{\Delta z_{Nz-1}}+Q_{Nz}^{n+1} \tag{S27}$$

Similarly, the Celia's method for the mixed form of the Richards equation will be:

$$-\frac{K_{w,Nz-1/2}^{n+1,m}}{\Delta z_{Nz-1}}h_{w,Nz-1}^{n+1,m+1}+\left(\frac{\Delta z_{Nz-1}}{2\Delta t}C_{Nz}^{n+1,m}+\frac{K_{w,Nz-1/2}^{n+1,m}}{\Delta z_{Nz-1}}\right)h_{w,Nz}^{n+1,m+1}=\frac{\Delta z_{Nz-1}}{2\Delta t}\left[C_{Nz}^{n+1,m}h_{w,Nz}^{n}-\left(\theta_{w,Nz}^{n+1,m}-\theta_{w,Nz}^{n}\right)\right]+\left(K_{w,Nz-1/2}^{n+1,m}-Q_{bottom}^{n+1}\right)+\frac{\Delta z_{Nz-1}}{2}Q_{Nz}^{n+1} \tag{S28}$$

B2. Air flow equation

$$\frac{\partial\rho_a\theta_a}{\partial t}+\frac{\partial\rho_a q_a}{\partial z}=Q \tag{S29}$$

$$\frac{\partial\rho_a\theta_a}{\partial t}+\frac{\partial\rho_a q_a}{\partial z}=Q\Rightarrow\frac{\rho_{ai-1/2}^{n+1}\theta_{ai-1/2}^{n+1}-\rho_{ai-1/2}^{n}\theta_{i-1/2}^{n}}{\Delta t}=\frac{-\rho_{ai-1}^{n+1}q_{ai-1}^{n+1}+\rho_{ai}^{n+1}q_{ai}^{n+1}}{\Delta z_i}+Q$$
$$\Rightarrow\rho_{ai-1}^{n+1}q_{ai-1}^{n+1}=\rho_{ai}^{n+1}q_{ai}^{n+1}+R_{vw}\Delta x-\frac{\Delta z_i}{\Delta t}\left(\rho_{ai}^{n+1}\theta_{ai}^{n+1}-\rho_{ai}^{n}\theta_i^n\right) \tag{S30}$$

Equation S30 shows the air flow equation can be solved by an explicit scheme by assuming the air flow velocity at the lower boundary of the soil is zero.

B3. Vapor flow (*Flux boundary condition*)

$$\frac{\partial\theta_a\rho_v}{\partial t}+\frac{\partial q_a\rho_v}{\partial z}=\frac{\partial}{\partial z}\left[\theta_a D_v\frac{\partial\rho_v}{\partial z}\right]+Q \tag{S31}$$

$$\beta Q_i^{n+1}+(1-\beta)Q_i^n=\frac{\rho_{v,i}^{n+1}\theta_{a,i}^{n+1}-\theta_{a,i}^{n}\rho_{v,i}^{n}}{\Delta t}+\beta\left\{\frac{\left(q_a\rho_v\right)_{i-1/2}^{n+1}-\left(q_a\rho_v\right)_{i+1/2}^{n+1}}{\Delta z}-\frac{1}{\Delta z}\left[\left(\theta_a D_v\right)_{i-1/2}^{n+1}\frac{\left(\rho_{\mathrm{v},i-1}^{n+1}-\rho_{v,i}^{n+1}\right)}{\Delta z_{i-1}}-\left(\theta_a D_v\right)_{i+1/2}^{n+1}\frac{\left(\rho_{v,i}^{n+1}-\rho_{v,i+1}^{n+1}\right)}{\Delta z_i}\right]\right\}$$
$$+(1-\beta)\left\{\frac{\left(q_a\rho_v\right)_{i-1/2}^{n}-\left(q_a\rho_v\right)_{i+1/2}^{n}}{\Delta z}-\frac{1}{\Delta z}\left[\left(\theta_a D_v\right)_{i-1/2}^{n}\frac{\left(\rho_{\mathrm{v},i-1}^{n}-\rho_{v,i}^{n}\right)}{\Delta z_{i-1}}-\left(\theta_a D_v\right)_{i+1/2}^{n}\frac{\left(\rho_{v,i}^{n}-\rho_{v,i+1}^{n}\right)}{\Delta z_i}\right]\right\} \tag{S32}$$

$$a_i h_{a,i-1}^{n+1}+b_i h_{a,i}^{n+1}+c_i h_{a,i+1}^{n+1}=e_i \tag{S33}$$

$$\begin{cases}a_i=\beta\left(\frac{q_{a,i-1}^{n+1}}{2}-\frac{\left(\theta_a D\right)_{i-1/2}^{n+1}}{\Delta z_{i-1}}\right)\\ b_i=\frac{\Delta z}{\Delta t}\theta_{a,i}^{n+1}+\beta\left(\frac{\left(\theta_a D\right)_{i-1/2}^{n+1}}{\Delta z_{i-1}}+\frac{\left(\theta_a D\right)_{i+1/2}^{n+1}}{\Delta z_i}\right) & i=[1,Nz-1]\\ c_i=\beta\left(-\frac{q_{a,i+1}^{n+1}}{2}-\frac{\left(\theta_a D\right)_{i+1/2}^{n+1}}{\Delta z_i}\right)\\ e_i=\frac{\Delta z}{\Delta t}\left[\theta_{a,i}^{n}\rho_{v,i}^{n}\right]+\Delta z Q_i^{n+1}+(1-\beta)\left\{\frac{\left(q_a\rho_v\right)_{i-1/2}^{n}-\left(q_a\rho_v\right)_{i+1/2}^{n}}{\Delta z}-\frac{1}{\Delta z}\left[\left(\theta_a D_v\right)_{i-1/2}^{n}\frac{\left(\rho_{\mathrm{v},i-1}^{n}-\rho_{v,i}^{n}\right)}{\Delta z_{i-1}}-\left(\theta_a D_v\right)_{i+1/2}^{n}\frac{\left(\rho_{v,i}^{n}-\rho_{v,i+1}^{n}\right)}{\Delta z_i}\right]\right\}\end{cases} \tag{S34}$$

Vapor density on the surface is evaluated by the evaporation rate:

$$\frac{\theta_{a,0}^{n+1}\rho_{v,0}^{n+1}-\theta_{a,0}^{n}\rho_{v,0}^{n}}{\Delta t}+2\left[\beta\frac{E_{sur}^{n+1}-q_{v1/2}^{n+1}}{\Delta z_0}+(1-\beta)\frac{E_{sur}^{n}-q_{v1/2}^{n}}{\Delta z_0}\right]=\beta Q_0^{n+1}+(1-\beta)Q_0^n \tag{S35}$$

$$\frac{\theta_{a,0}^{n+1}\rho_{v,0}^{n+1}-\theta_{a,0}^{n}\rho_{v,0}^{n}}{\Delta t}=\beta\frac{\frac{\rho_{v,0}^{n+1}u_{a0}^{n+1}+\rho_{v,1}^{n+1}u_{a1}^{n+1}}{2}-\left(\theta_a D_v\right)_{1/2}^{n+1}\frac{\left(\rho_{v,0}^{n+1}-\rho_{v,1}^{n+1}\right)}{\Delta z_0}-E_{sur}^{n+1}}{\Delta z_0/2}+(1-\beta)\frac{\frac{\rho_{v,0}^{n}u_{a0}^{n}+\rho_{v,1}^{n}u_{a1}^{n}}{2}-\left(\theta_a D_v\right)_{1/2}^{n}\frac{\left(\rho_{v,0}^{n}-\rho_{v,1}^{n}\right)}{\Delta z_0}-E_{sur}^{n}}{\Delta z_0/2}$$
$$+\beta Q_0^{n+1}+(1-\beta)Q_0^n \tag{S36}$$

Bottom boundary: zero gradient

$$\frac{\rho_{v,Nz}^{n+1}\theta_{a,Nz}^{n+1}-\rho_{v,Nz}^{n}\theta_{a,Nz}^{n}}{\Delta t}=2\frac{-\left[\frac{(\rho_v u_a)_{Nz-1}^{n+1}+(\rho_v u_a)_{Nz}^{n+1}}{2}-(\theta_a D_v)_{Nz-1/2}^{n+1}\frac{(\rho_{v,Nz-1}^{n+1}-\rho_{v,Nz}^{n+1})}{\Delta z_{Nz-1}}\right]+(\rho_v u_a)_{Nz}^{n+1}}{\Delta z_{Nz-1}}+Q_{Nz}^{n+1} \tag{S37}$$

B4. Heat flow

$$\begin{cases}\dfrac{\partial C_{eq}T}{\partial t}+\dfrac{\partial u_H T}{\partial z}=\dfrac{\partial}{\partial z}\left[\lambda\dfrac{\partial T}{\partial z}\right]-Q\\ u_H=c_w\rho_w q_w+c_a\rho_a q_a+\theta_a J_{hG}\left(c_v-c_{a,dry}\right)\\ C_{eq}=\theta_w\rho_w c_w+\theta_a\rho_a c_a+(1-\phi)\rho_s c_s\end{cases} \tag{S38}$$

$$\begin{aligned}&\frac{C_i^{n+1}T_i^{n+1}-C_i^{n}T_i^{n}}{\Delta t}=\beta\left\{-\frac{u_{H,i-1/2}^{n+1}T_{i-1/2}^{n+1}-u_{H,i+1/2}^{n+1}T_{i+1/2}^{n+1}}{\Delta z}+\frac{1}{\Delta z}\left[\lambda_{i-1/2}^{n+1}\frac{(T_{i-1}^{n+1}-T_i^{n+1})}{\Delta z_{i-1}}-\lambda_{i+1/2}^{n+1}\frac{(T_i^{n+1}-T_{i+1}^{n+1})}{\Delta z_i}\right]\right\}\\ &(1-\beta)\left\{-\frac{u_{H,i-1/2}^{n}T_{i-1/2}^{n}-u_{H,i+1/2}^{n}T_{i+1/2}^{n}}{\Delta z}+(1-\beta)\frac{1}{\Delta z}\left[\lambda_{i-1/2}^{n}\frac{(T_{i-1}^{n}-T_i^{n})}{\Delta z_{i-1}}-\lambda_{i+1/2}^{n}\frac{(T_i^{n}-T_{i+1}^{n})}{\Delta z_i}\right]\right\}-\Delta z Q_i^{n+1}\end{aligned} \tag{S39}$$

$$\begin{cases}a_i h_{a,i-1}^{n+1}+b_i h_{a,i}^{n+1}+c_i h_{a,i+1}^{n+1}=e_i\\ a_i=\beta\left[\dfrac{u_{H,i-1}^{n+1}}{2}-\dfrac{\lambda_{i-1/2}^{n+1}}{\Delta z_{i-1}}\right]\\ b_i=\dfrac{\Delta z}{\Delta t}C_{\mathrm{eq},i}^{\,n+1}+\beta\left[\dfrac{\lambda_{i-1/2}^{n+1}}{\Delta z_{i-1}}+\dfrac{\lambda_{i+1/2}^{n+1}}{\Delta z_i}\right] \qquad i=[1,Nz-1]\\ c_i=\beta\left[-\dfrac{u_{H,i+1}^{n+1}}{2}-\dfrac{\lambda_{i+1/2}^{n+1}}{\Delta z_i}\right]\\ e_i=\dfrac{\Delta z}{\Delta t}C_i^{n}T_i^{n}-\Delta z\dfrac{Q_i^{n}+Q_i^{n+1}}{2}+(1-\beta)\left[-\dfrac{\left(u_{H,i-1}^{n}T_{i-1}^{n}-u_{H,i+1}^{n}T_{i+1}^{n}\right)}{2}+\lambda_{i-1/2}^{n}\dfrac{(T_{i-1}^{n}-T_i^{n})}{\Delta z_{i-1}}-\lambda_{i+1/2}^{n}\dfrac{(T_i^{n}-T_{i+1}^{n})}{\Delta z_i}\right]\end{cases} \tag{S40}$$

Surface boundary: heat flux boundary

If we set the surface potential head as H_{sur}, the potential head of the first node of soil profile is $h_0=H_{sur}$, thus, the first function is expressed as:

$$\frac{C_0^{n+1}T_0^{n+1}-C_0^{n}T_0^{n}}{\Delta t}=2\frac{Q_{1/2}+Q_{sur}}{\Delta z_0}-Q \tag{S41}$$

$$\frac{C_0^{n+1}T_0^{n+1}-C_0^{n}T_0^{n}}{\Delta t}=\frac{\left[U_{H1/2}^{n+1}T_{1/2}^{n+1}-\lambda_{1/2}^{n+1}\dfrac{T_0^{n+1}-T_1^{n+1}}{\Delta z_0}\right]+E_{rain}+Q_{sur}}{\Delta z_0/2}-Q \tag{S42}$$

Lower boundary: zero gradient boundary

$$\frac{C_{Nz}^{n+1}T_{Nz}^{n+1}-C_{Nz}^{n}T_{Nz}^{n}}{\Delta t}=\frac{-Q_{Nz-1/2}-Q_{bot}}{\Delta z}-Q \tag{S43}$$

$$\frac{C_{Nz}^{n+1}T_{Nz}^{n+1}-C_{Nz}^{n}T_{Nz}^{n}}{\Delta t}=\frac{-u_{H,Nz-1/2}^{n+1}T_{Nz-1/2}^{n+1}+\lambda_{Nz-1/2}^{n+1}\dfrac{(T_{Nz-1}^{n+1}-T_{Nz}^{n+1})}{\Delta z_{Nz-1}}-Q_{bot}}{\Delta z_{Nz-1}/2}-Q_{Nz}^{n+1} \tag{S44}$$